Manipulation of strain state in silicon nanoribbons by top-down approach

Zhiqiang Mu, Miao Zhang, Zhongying Xue, Gaodi Sun, Qinglei Guo, Da Chen, Gaoshan Huang, Yongfeng Mei, Paul K. Chu, Zengfeng Di, and Xi Wang

Citation: Appl. Phys. Lett. **106**, 174102 (2015); doi: 10.1063/1.4919630
View online: https://doi.org/10.1063/1.4919630
View Table of Contents: http://aip.scitation.org/toc/apl/106/17
Published by the American Institute of Physics

APPLIED PHYSICS LETTERS 106, 174102 (2015)

Manipulation of strain state in silicon nanoribbons by top-down approach

Zhiqiang Mu,[1] Miao Zhang,[1] Zhongying Xue,[1] Gaodi Sun,[1] Qinglei Guo,[1] Da Chen,[1] Gaoshan Huang,[2] Yongfeng Mei,[2] Paul K. Chu,[3] Zengfeng Di,[1,a)] and Xi Wang[1]
[1]*State Key Laboratory of Functional Materials for Informatics, Shanghai Institute of Microsystem and Information Technology, Chinese Academy of Sciences, Shanghai 200050, China*
[2]*Department of Materials Science, Fudan University, Shanghai 200433, China*
[3]*Department of Physics and Materials Science, City University of Hong Kong, Tat Chee Avenue, Kowloon, Hong Kong, China*

(Received 14 January 2015; accepted 21 April 2015; published online 1 May 2015)

Tensile strain is often utilized to enhance the electron mobility and luminescent characteristics of semiconductors. A top-down approach in conjunction with roll-up technology is adopted to produce high tensile strain in Si nanoribbons by patterning and releasing of the bridge-like structures. The tensile strain can be altered between uniaxial state and biaxial state by adjusting the dimensions of the patterns and can be varied controllably up to 3.2% and 0.9% for the uniaxial- and biaxial-strained Si nanoribbons, respectively. Three-dimensional finite element analysis is performed to investigate the mechanism of strain generation during patterning and releasing of the structure. Since the process mainly depends on the geometrical factors, the technique can be readily extended to other types of mechanical, electrical, and optical membranes. © *2015 AIP Publishing LLC*.
[http://dx.doi.org/10.1063/1.4919630]

Introduction of tunable strain to semiconductors offers the possibility to tune the physical properties of microelectronic[1,2] and optoelectronic[3,4] devices such as the electronic band structure and charge transport to enhance the performance. In particular, owing to the compatibility with the mainstream integrated circuit (IC) technology, strain engineering is widely explored for group IV semiconductors. For instance, Si nanowires with high uniaxial tensile strain have been produced using strained silicon-on-insulator (sSOI).[5,6] By patterning the top strained Si layer into dumb-bell bridges and relaxing them, the built-in tensile strain in the sSOI transforms from the initial biaxial state to uniaxial-tensile one. Enhancement of the electron mobility has been demonstrated from uniaxial tensile strained Si nanowire metal-oxide-semiconductor field-effect transistors (MOSFETs).[7] By means of the strain transformation approach, the minor biaxial tensile strain in Ge (as low as $\sim$0.2%) due to the mismatch of the thermal expansion coefficients between Ge and Si can create considerable uniaxial tensile strain, which is even sufficient to convert the indirect bandgap of Ge into a direct one. By adoption of such strain engineering, the efficient light emission from Ge becomes possible.[8–11] However, strain engineering for sSOI and Ge epitaxy requires that the tensile strain pre-exists in the initial substrate. Alternatively, using SiGe and Si_3N_4 stressors, the process-induced strain starting from the strain-free substrate has been implemented to induce compressive and tensile strain in PMOS and NMOS channel regions to increase the drive currents of the devices, respectively.[12,13] Meanwhile, roll-up nanotechnology has been proven to be effective in introducing uniaxial strain into strain-free semiconductor nanomembranes.[14–16] Nevertheless, the process-induced strain is always uniaxial and creation of biaxial strain has seldom been reported even though the performances of microelectronic or optoelectronic devices under biaxial tensile strain is more significant than that under the uniaxial condition.[17–19]

Herein, by adopting the roll-up nanotechnology, a technique started from strain-free substrate is described to produce both uniaxial- and biaxial-tensile strained Si nanoribbons. The strain state and distribution of the strained Si nanoribbons are investigated by micro-Raman scattering and finite element method (FEM) analysis is performed to obtain insights into the strain generation mechanism during patterning and production of the structures.

A 50 nm thick tungsten (W) layer with 2.2 GPa built-in tensile stress was deposited on a 150-mm strain-free (100) SOI wafer with a 50 nm thick Si layer and 120 nm thick buried silicon dioxide (BOX) by magnetron sputtering (the value of tensile stress is pre-estimated based on the warp measurement[20]). Standard ultraviolet lithography and wet chemical etching were employed to define the W pads. A second lithographic process employing inductively coupled plasma (ICP) was performed to define the [100] Si pads and bridges aligned to the W pad structures. The Si bridge structure was produced by selective etching of the BOX layer using hydrofluoric acid (HF). Owing to the built-in tensile stress in the W layer, the pad composed of the W/Si bilayer rolls up after HF etching and CO_2 supercritical-point drying, as demonstrated in Figure 1(a). Since the W/Si pad (width of 30 μm and length of 100 μm) was larger than the connected Si nanoribbon bridge (width of 1 μm and length of 10 μm), the connected Si bridge was severely stretched by the rolled-up W/Si pad thus generating a considerable amount of uniaxial-tensile strain (Figure 1(b)). To convert the uniaxial-tensile strain to biaxial-tensile strain, a special pattern consisting of four W/Si pads connected to the Si cross-bridge was designed. When the pattern was released from the SOI substrate by HF etching, four W/Si pads were rolled up

a)Author to whom correspondence should be addressed. Electronic mail: zfdi@mail.sim.ac.cn

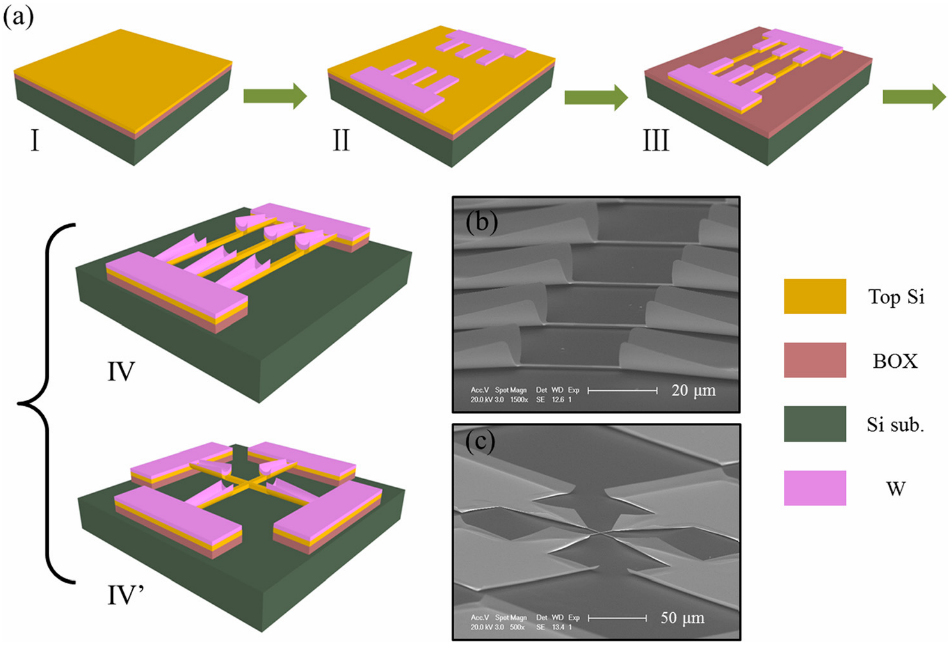

FIG. 1. (a) Process flow for the fabrication of uniaxially/biaxially strained Si nanoribbons; (b) SEM image of Si nanoribbons with uniaxial-tensile strain; and (c) SEM image of Si nanoribbons with biaxial-tensile strain.

simultaneously and the intersection region of the Si cross-bridge was stretched from both orthogonal directions to create the biaxial-tensile strain as shown in Figure 1(c).

As a non-destructive technique to evaluate strain in crystals and films, micro-Raman line-scan measurement using 325 nm He-Cd laser is performed along the transverse direction of the Si bridge to characterize the strain distribution (Figure 2(a)). The laser spot size of micro-Raman system is $\sim$0.8 μm, and the lateral (XY) spatial resolution is $\sim$0.4 μm. The typical Raman peak at 520.7 cm^{-1} is attributed to the Si-Si longitudinal-optical phonon mode from the bottom Si layer of the SOI substrate. In the Si nanoribbon area, a Raman peak at a smaller wavenumber suggesting the existence of tensile strain in the Si bridge is detected. The uniaxial-tensile strain $\varepsilon_{\mathrm{uniaxial}}$ in the Si bridge is determined by the following equation:[21]

$$\varepsilon_{\mathrm{uniaxial}}(\%) = -0.399 \times (\omega_{\mathrm{bulk}} - \omega_{\mathrm{strained}}) \qquad (1)$$

where the negative sign represents tensile strain, 0.399 is the strain-shift coefficient for uniaxial strain (cm), and ω_{bulk} and $\omega_{\mathrm{strained}}$ represent the peak positions of the Si-Si vibration mode of the bulk Si and strain Si, respectively. With regard to the 2 μm wide Si bridge, the Raman shift $\Delta\omega$ ($\Delta\omega = \omega_{\mathrm{bulk}} - \omega_{\mathrm{strained}}$) is as large as 6.5 cm^{-1}, which corresponds to 2.6% uniaxial tensile strain. To analyze the strain uniformity in the Si bridge, Raman line-scans are acquired along the longitudinal directions of the two Si nanoribbons with widths of 1 and 2 μm, as shown in Figure 2(b). The strain distributions along the Si bridges are quite uniform showing fluctuations of only $\pm$3.8% and $\pm$5.6% for the 1 and 2 μm wide Si bridges, respectively. In addition, the tensile strain increases from 2.6% to 3.2% as the width of the Si bridge decreases from 2 μm to 1 μm. It should be noted that the artificial Raman shift towards a smaller wavenumber is always observed from suspended structures as a result of the laser heating effect since the thermal dissipation is retarded by the air gaps.[22,23] In this study, power-dependent Raman spectra analysis proposed by Süess[24] is performed to estimate the laser heating of the suspended structures. However, the thermal effect-induced Raman shift in this study seems more significant due to the wider air gap. The Raman peaks shift to

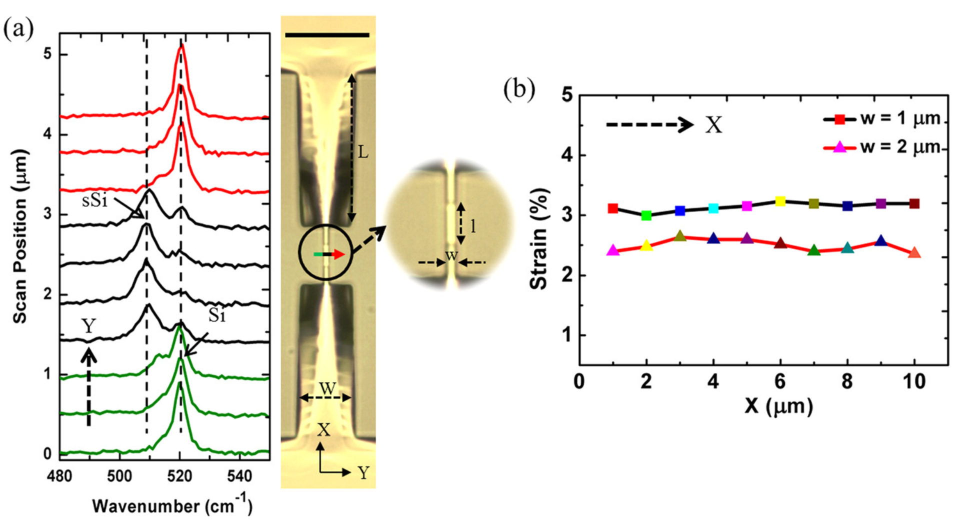

FIG. 2. (a) Raman line scans of the Si nanoribbon bridge 10 μm long and 2 μm wide. An optical picture of the measured structure is displayed on the right and the scale bar being 50 μm. (b) Uniaxial-tensile strain along the Si nanoribbon bridges 1 and 2 μm wide.

smaller wavenumbers as the laser power is increased, indicating that the temperature of the suspended Si bridge is sensitive to the power of the excitation laser (not shown here). When the laser power is confined to within 1%–5% of the total power density of the excitation laser, the variation in the Raman shift is negligible. Therefore, a laser power as small as 1% of the total power density (corresponding to the power of less than 90 μW) is chosen for the strain evaluation in our experiments to eliminate the laser heating effect.

The strain degree in the Si nanoribbon bridge connected by W/Si pads with different geometrical dimensions is studied systematically. The uniaxial-tensile strain of the $2\,\mu m \times 10\,\mu m$ Si bridges with different W/Si pad widths and fixed pad length of 50 μm is shown in Figure 3(a). As the width of the pad is increased from 10 μm to 32 μm, the Raman peaks shift toward lower wavenumbers indicating higher tensile strain. With regard to the 10 μm wide pad, the Raman peak of the Si nanoribbon bridge is located at 518.5 cm^{-1}, corresponding to uniaxial tensile strain of 0.88%. As the pad width is increased to 32 μm, the Raman peak of the Si bridge moves to 515.3 cm^{-1} which corresponds to 2.15% uniaxial tensile strain. The Raman shifts of the Si bridges with identical geometrical dimensions but connected with 32 μm-wide W/Si pads of different lengths are summarized in Figure 3(b). As the pad length is increased from 20 μm to 100 μm, the uniaxial tensile strain of the Si bridge increases from 1.4% to 2.9% accordingly. As aforementioned, when the width of the Si bridge shrinks to 1 μm, uniaxial tensile strain as high as 3.2% can be obtained. It is believed that the uniaxial tensile strain can be further improved by reducing the width of the Si nanoribbon bridge to the sub-μm scale. Nonetheless, the tensile strain obtained by this method is remarkably high compared to other stress techniques. For instance, as the mainstream technique in strain engineering in the microelectronics industry, a Si_3N_4 stressor layer is commonly used to generate the tensile strain in Si channel, thus increasing the electron mobility in n-type MOSFETs. However, it is still challenging to obtain uniaxial tensile strain larger than 1.2%.[1,25] Our approach enables fine tuning of the uniaxial tensile strain by varying the dimensions of the structural components, that is, lengths and widths of both the pads and the bridges.

In addition to the Si bridge with uniaxial-tensile strain, we extend our approach to fabricate a suspended structure with biaxial-tensile strain by integrating two orthogonal $1\,\mu m \times 10\,\mu m$ Si bridges, as illustrated in Figure 1(c). Raman mapping is performed to characterize the strain distribution in the nanoribbons including the uniaxial and biaxial parts. As shown in Figure 4(a), the Raman shifts of both Si bridges are rather uniform, except the boundary area between the uniaxial and biaxial parts involving shear force. For the biaxial-tensile strain, $\varepsilon_{biaxial}$, the strain in the Si bridge is evaluated by the following equation:[21]

$$\varepsilon_{biaxial}(\%) = -0.144 \times (\omega_{bulk} - \omega_{strained}) \quad (2)$$

where 0.144 is the strain-shift coefficient for biaxial strain (cm). According to Eqs. (1) and (2), the tensile strain profile of the Si cross-bridge is deduced and displayed in Figure 4(b). The biaxial-tensile strain of 0.9% is uniformly distributed at the intersection of the Si cross-bridge.

Three-dimensional FEM simulation with COMSOL Multiphysics of linear elastic mechanics is performed to analyze the displacement and strain distribution of the suspended Si bridges. A 50 nm thick W layer with 2.2 GPa built-in tensile stress and 50 nm thick stress-free (100) Si nanomembrane are modeled based on the experimental structures. The W and Si layers are set as isotropic and anisotropic, respectively. The side boundaries connected to the bigger pads in the experimental structures are fixed rigidly. As discussed previously,[15] the membranes with nanometers thick released from the substrate bend or roll up if there is a built-in strain gradient across the film thickness and the roll-up process is guided by energy minimization. As shown in Figure 4(c), rolling-up of the W/Si pads is driven by the built-in tensile stress producing the out-of-plane displacement. In addition, the out-of-plane displacement of the Si cross-bridge is uniform and relatively small compared to the W/Si pads. Owing to the rolling-up of the four W/Si pads, the intersection of the Si cross-bridge is stretched from two orthogonal directions, thus yielding the biaxial-tensile strain (the cyan-blue area shown in Figure 4(d)). Meanwhile, the other areas maintain the uniaxial tensile strain, as shown by the uniform orange color in Figure 4(d). FEM simulation also indicates that the strain field distribution within the cross section of the Si bridge is rather uniform (not shown).

It is well known that the electron mobility enhancement under biaxial tensile strain is more significant than that under the uniaxial condition and it is believed to be caused by a larger fraction of in-plane electrons with smaller effective masses and smaller fraction of out-of-plane electrons with higher effective mass.[17,18] In addition, by means of first-

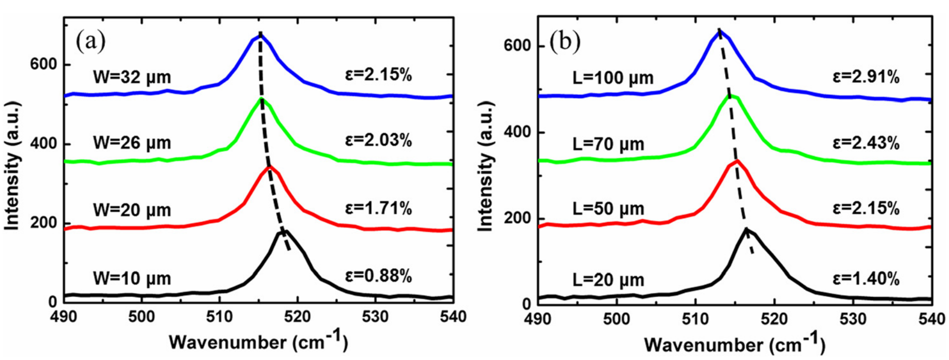

FIG. 3. Raman spectra of the $2\,\mu m \times 10\,\mu m$ uniaxial tensile strained Si nanoribbons: (a) 50 μm-long W/Si pads with different widths and (b) 32 μm-wide W/Si pads with different lengths.

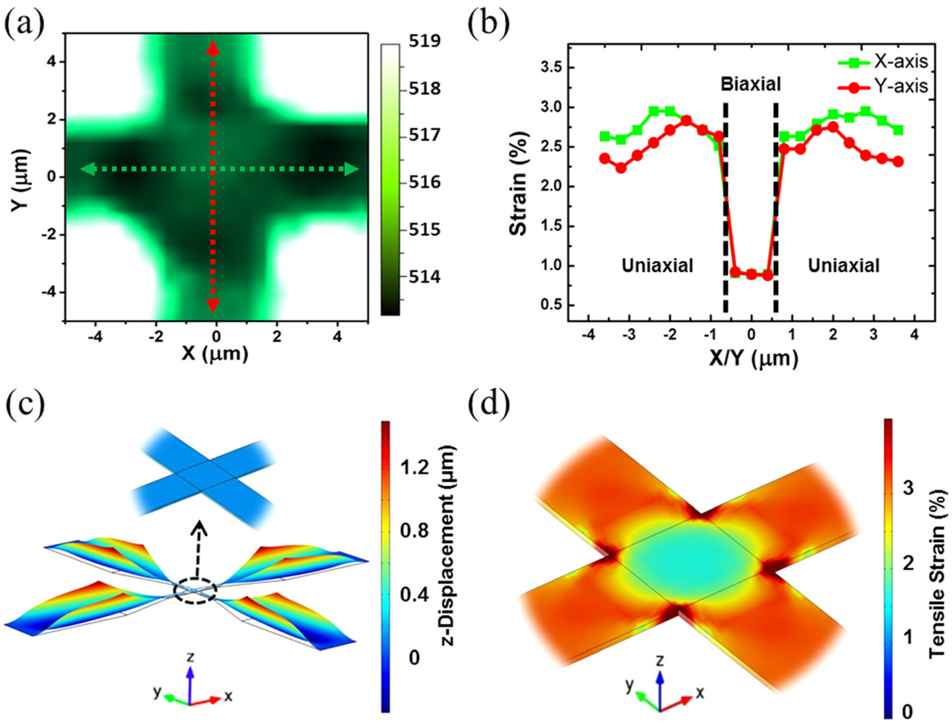

FIG. 4. (a) Raman mapping measurement of Si cross-bridge. (b) Tensile strain profile of the Si cross-bridge along the X and Y axes. (c) FEM simulation of the out-of-plane displacement of the rolled-up W/Si pads connected to the cross-bridge. (d) FEM simulation of the uniaxial and biaxial tensile strain distributions of the Si cross-bridge.

principles calculation, it is found that the biaxial tensile strain is more efficient in converting Ge into direct bandgap than uniaxial tensile strain.[19] Therefore, the proposed approach may provide a potential way to create biaxial tensile strain which can improve the performance of microelectronic or optoelectronic devices more effectively.

In summary, a top-down fabrication technique is demonstrated to produce tensile strained Si nanoribbons by patterning and releasing the bridge-like structures. Uniaxial strain as high as 3.2% and biaxial strain as high as 0.9% can be obtained by adjusting the geometry of the pattern from a single-bridge structure to crossed-bridge one. The strain state and value can be tailored by designing the patterns with different geometric parameters. Since the outcome depends only on the geometric factors, this method can be readily extended to other microelectronic and optoelectronic membrane structures.

This work was financially supported from Creative Research Groups of National Natural Science Foundation of China (No. 61321492), National Natural Science Foundation of China under Grant Nos. 61176001, 51222211, 51322201, and 61274136, Chinese Academy of Sciences (CAS) International Collaboration and Innovation Program on High Mobility Materials Engineering, and City University of Hong Kong Strategic Research Grant (SRG) No. 7004188.

[1]M. Chu, Y. K. Sun, U. Aghoram, and S. E. Thompson, Annu. Rev. Mater. Res. **39**, 203 (2009).
[2]S. Baudot, F. Andrieu, O. Faynot, and J. Eymery, Solid-State Electron. **54**, 861 (2010).
[3]A. Ghrib, M. El Kurdi, M. de Kersauson, M. Prost, S. Sauvage, X. Checoury, G. Beaudoin, I. Sagnes, and P. Boucaud, Appl. Phys. Lett. **102**, 221112 (2013).
[4]H. S. Lan, S. T. Chan, T. H. Cheng, C. Y. Chen, S. R. Jan, and C. W. Liu, Appl. Phys. Lett. **98**, 101106 (2011).
[5]R. A. Minamisawa, M. J. Suess, R. Spolenak, J. Faist, C. David, J. Gobrecht, K. K. Bourdelle, and H. Sigg, Nat. Commun. **3**, 1096 (2012).
[6]G. D. Sun, M. Zhang, Z. Y. Xue, Q. L. Guo, D. Chen, Z. Q. Mu, L. X. Dong, X. Wang, and Z. F. Di, Appl. Phys. Lett. **105**, 193505 (2014).
[7]G. V. Luong, L. Knoll, S. Blaeser, M. J. Süess, H. Sigg, A. Schäfer, S. Trellenkamp, K. K. Bourdelle, D. Buca, Q. T. Zhao, and S. Mantl, Solid-State Electron. **108**, 19 (2015).
[8]D. Nam, D. S. Sukhdeo, S. Gupta, J.-H. Kang, M. L. Brongersma, and K. C. Saraswat, IEEE J. Sel. Top. Quantum Electron. **20**, 1500107 (2014).
[9]D. Nam, D. S. Sukhdeo, J.-H. Kang, J. Petykiewicz, J. H. Lee, W. S. Jung, J. Vuckovic, M. L. Brongersma, and K. C. Saraswat, Nano Lett. **13**, 3118 (2013).
[10]M. J. Süess, R. Geiger, R. A. Minamisawa, G. Schiefler, J. Frigerio, D. Chrastina, G. Isella, R. Spolenak, J. Faist, and H. Sigg, Nat. Photonics **7**, 466 (2013).
[11]D. S. Sukhdeo, D. Nam, J.-H. Kang, M. L. Brongersma, and K. C. Saraswat, Photonics Res. **2**, A8 (2014).
[12]T. Ghani, M. Armstrong, C. Auth, M. Bost, P. Charvat, G. Glass, T. Hoffmann, K. Johnson, C. Kenyon, J. Klaus, B. McIntyre, K. Mistry, A. Murthy, J. Sandford, M. Silberstein, S. Sivakumar, P. Smith, K. Zawadzki, S. Thompson, and M. Bohr, Tech. Dig. - Int. Electron Devices Meet. **2003**, 11.6.1.
[13]C. Auth, C. Allen, A. Blattner, D. Bergstrom, M. Brazier, M. Bost, M. Buehler, V. Chikarmane, T. Ghani, T. Glassman, R. Grover, W. Han, D. Hanken, M. Hattendorf, P. Hentges, R. Heussner, J. Hicks, D. Ingerly, P. Jain, S. Jaloviar, R. James, D. Jones, J. Jopling, S. Joshi, C. Kenyon, H. Liu, R. McFadden, B. McIntyre, J. Neirynck, C. Parker, L. Pipes, I. Post, S. Pradhan, M. Prince, S. Ramey, T. Reynolds, J. Roesler, J. Sandford, J. Seiple, P. Smith, C. Thomas, D. Towner, T. Troeger, C. Weber, P. Yashar, K. Zawadzki, and K. Mistry, Symp. VLSI Technol., Dig. Tech. Pap. **2012**, 131.
[14]Y. F. Mei, G. S. Huang, A. A. Solovev, E. B. Urena, I. Moench, F. Ding, T. Reindl, R. K. Y. Fu, P. K. Chu, and O. G. Schmidt, Adv. Mater. **20**, 4085 (2008).
[15]J. X. Li, J. Zhang, W. Gao, G. S. Huang, Z. F. Di, R. Liu, J. Wang, and Y. F. Mei, Adv. Mater. **25**, 3715 (2013).
[16]G. S. Huang and Y. F. Mei, Adv. Mater. **24**, 2517 (2012).
[17]R. Tanabe, T. Yamasaki, Y. Ashizawa, and H. Oka, J. Comput. Electron. **6**, 49 (2007).
[18]K. Uchida, R. Zednik, L. Ching-Huang, H. Jagannathan, J. McVittie, P. C. McIntyre, and Y. Nishi, Tech. Dig. - Int. Electron Devices Meet. **2004**, 229.
[19]L. Liu, M. Zhang, L. J. Hu, Z. F. Di, and S. J. Zhao, J. Appl. Phys. **116**, 113105 (2014).

[20]N. R. Draney, J. L. Jun, and T. Jiang, IEEE Workshop Microelectron. Electron Devices **2004**, 120.
[21]M. Kurosawa, T. Sadoh, and M. Miyao, Appl. Phys. Lett. **98**, 012110 (2011).
[22]S. Piscanec, M. Cantoro, A. C. Ferrari, J. A. Zapien, Y. Lifshitz, S. T. Lee, S. Hofmann, and J. Robertson, Phys. Rev. B **68**, 241312 (2003).
[23]K. W. Adu, H. R. Gutierrez, U. J. Kim, and P. C. Eklund, Phys. Rev. B **73**, 155333 (2006).
[24]M. J. Süess, R. A. Minamisawa, R. Geiger, K. K. Bourdelle, H. Sigg, and R. Spolenak, Nano Lett. **14**, 1249 (2014).
[25]S. E. Thompson, G. Y. Sun, Y. S. Choi, and T. Nishida, IEEE Trans. Electron Devices **53**, 1010 (2006).